Viitanen, Ville M.; Sipilä, Tuomas; Sánchez-Caja, Antonio; Siikonen, Timo

Compressible two-phase viscous flow investigations of cavitation dynamics for the ittc standard cavitator

Published in:
Applied Sciences (Switzerland)

DOI:
10.3390/app10196985

Published: 07/10/2020

Document Version
Publisher's PDF, also known as Version of record

applied sciences

MDPI

Article

Compressible Two-Phase Viscous Flow Investigations of Cavitation Dynamics for the ITTC Standard Cavitator

Ville M. Viitanen [1,*], Tuomas Sipilä [2], Antonio Sánchez-Caja [1] and Timo Siikonen [3]

[1] VTT Technical Research Centre of Finland Ltd., 02150 Espoo, Finland; antonio.sanchez@vtt.fi
[2] ABB Marine and Ports, 00980 Helsinki, Finland; tuomas.sipila@fi.abb.com
[3] Department of Mechanical Engineering, Aalto University, 02150 Espoo, Finland; timo.siikonen@aalto.fi
* Correspondence: ville.viitanen@vtt.fi

Received: 4 September 2020; Accepted: 28 September 2020; Published: 7 October 2020

Featured Application: The present method can be applied to study characteristics of hydrodynamic cavitation and its consequences, such as performance variations and noise, in propellers and rotating turbomachinery. Compressible formulation of the numerical method ensures a more precise treatment of the multiphase flow dynamics, and can reveal some interesting physical phenomena due to the cavitation. Accurate prediction of the multiphase flow is a requisite for optimal, efficient and environmentally friendly design and operation of such devices.

Abstract: In this paper, the ITTC Standard Cavitator is numerically investigated in a cavitation tunnel. Simulations at different cavitation numbers are compared against experiments conducted in the cavitation tunnel of SVA Potsdam. The focus is placed on the numerical prediction of sheet-cavitation dynamics and the analysis of transient phenomena. A compressible two-phase flow model is used for the flow solution, and two turbulence closures are employed: a two-equation unsteady RANS model, and a hybrid RANS/LES model. A homogeneous mixture model is used for the two phases. Detailed analysis of the cavitation shedding mechanism confirms that the dynamics of the sheet cavitation are dictated by the re-entrant jet. The break-off cycle is relatively periodic in both investigated cases with approximately constant shedding frequency. The CFD predicted sheet-cavitation shedding frequencies can be observed also in the acoustic measurements. The Strouhal numbers lie within the usual ranges reported in the literature for sheet-cavitation shedding. We furthermore demonstrate that the vortical flow structures can in certain cases develop striking cavitating toroidal vortices, as well as pressure wave fronts associated with a cavity cloud collapse event. To our knowledge, our numerical analyses are the first reported for the ITTC standard cavitator.

Keywords: hydrodynamic cavitation; compressible two-phase flow; turbulence modelling; system instabilities

1. Introduction

Cavitation, when it occurs, is a cause of many detrimental effects on marine propellers and turbomachinery. Apart from performance degradation, it may trigger erosion, cause vibration problems, or result in high-intensity noise emission on a broad frequency range. Different types of cavitation involve complex features such as bubbly flow, bubble coalescence, nucleation, free-surface instability, and turbulence. These features do not necessarily obey a single but multiple length and time scales, which renders their reliable prediction, either experimentally or numerically, a major undertaking. For instance, when investigating the performance of marine propellers, depending on their operating conditions, many different forms of cavitation can take place simultaneously, such as

steady attached sheet cavitation near the blade's leading edge, cloud cavitation in the propeller's wake, and vortex cavitation originating from the blade tips and the propeller hub.

Even in the case of steady uniform inflow conditions, we can observe unsteady behavior of the cavitation. In particular, the shedding behavior of sheet cavitation (Figure 1) and its subsequent transformation to cloudy and bubbly cavities are important in the generation of the aforementioned erosion and noise issues, since upon collapsing these cavitation types can yield strong pressure fluctuations and even shock waves in the bubbly mixture or in the liquid phase [1,2]. A sketch of the shedding cycle of two-dimensional sheet cavitation is shown in Figure 1. The first frames depict the growth of the attached sheet cavity following the break-off of the previous sheet. The growth will cease after a certain length of the sheet cavity, and a strong re-entrant jet is formed at the closure of the sheet cavity, as depicted in Frame 3. The following frame shows the impingement of the cavity interface by the jet, as the jet reaches the cavity near the leading edge. The rear part of the sheet cavity breaks off and reduces to a bubble cloud, which is convected downstream as shown in Frame 5. As the cloud travels downstream, parts of it may undergo a violent collapsing stage, possibly causing noise and material erosion. Meanwhile, as seen in Frame 6, the newly formed sheet cavity on the foil behind the LE will begin to grow, initiating a subsequent break-off cycle.

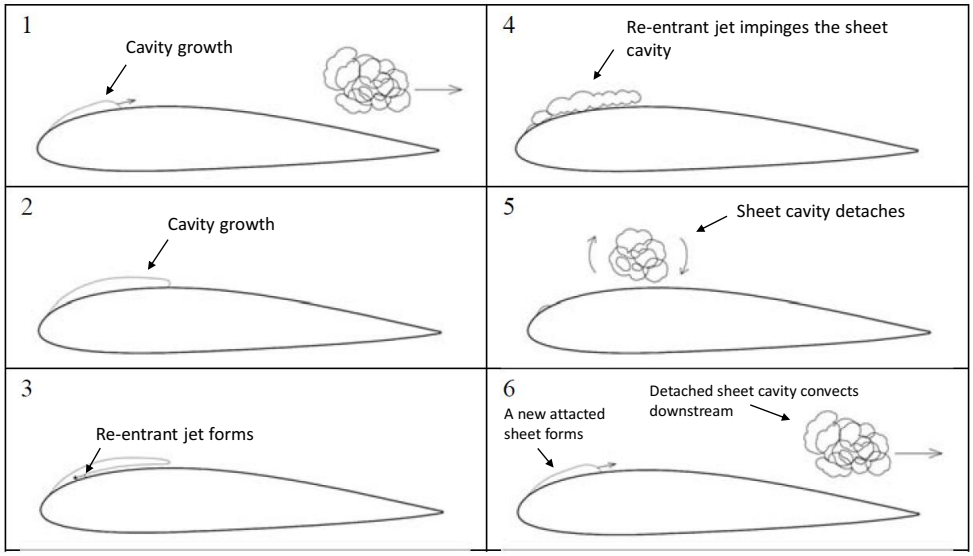

Figure 1. Sketch of the shedding mechanism of sheet cavitation. The figure illustrates one break-off cycle, adapted from [3].

The dynamics of the sheet cavitation are mainly determined by the re-entrant jet, although a bubbly shock wave can in certain conditions affect this development [1]. If the sheet cavity is thick, the break-off cycle is relatively periodic with approximately constant shedding frequency. In these cases, a Strouhal number $St = fl_{ref}/U_{ref}$ can be determined. The length scale of the Strouhal number is chosen as the maximum length of the cavity. This can be argued to be a typical length scale of the cavity since the shedding frequency depends on the distance the re-entrant jet has to travel. The choice of the velocity scale is somewhat problematic, but can be taken as the free-stream velocity $U_{ref} = U_\infty$, or based on an approximation of the re-entrant jet velocity $U_{ref} = U_\infty\sqrt{1+\sigma}$, where σ is the cavitation number, which acknowledges the presence of a cavity structure in a better way than U_∞ alone [4]. The frequency, f, is based on global shedding of the cavity clouds, determined with a visual inspection of the cavity shedding periodicity, with the help of time histories of the measured lift and drag forces. Typically, the Strouhal numbers for sheet-cavitation shedding vary as $0.20 \ldots 0.50$, depending on the investigated conditions and the definition for the reference quantities [4–7].

In frames 5–6 of Figure 1 we observe that the detached cavity clouds convect downstream toward a higher-pressure region. Upon reaching the regions of sufficiently higher ambient pressure, the detached

cavity clouds likely undergo a violent collapsing stage. Collapse events of cavitation structures behind a ship's propeller, for instance, can lead to very high-pressure peaks, and such peaks can exhibit very rapid temporal variation. As noted by Matusiak [8], a primary source of high-frequency noise is the collapse of the free cavitation bubbles. The shedding behavior is mainly governed by the development of the re-entrant jet, vortical structures and turbulent flow near the foil, i.e., the unsteady dynamics of especially the liquid phase. As Reynolds-averaged Navier–Stokes (RANS) equations are mainly derived for steady single-phase flows, complex unsteady phenomena may be severely under-predicted when using an unsuitable turbulence-modelling approach. High-fidelity turbulence modelling is typically needed to capture a detailed flow field for the prediction of the dynamics of cavitation and its consequences such as erosion and noise [9–12]. Therefore in this study, we employ two different turbulence closures: an unsteady RANS-based SST $k-\omega$ turbulence model and a hybrid RANS/LES (large eddy simulation) closure called the delayed-detached eddy simulation (DDES). We analyze the two-phase flow using a compressible multiphase model. Cavitating problems have been typically treated with incompressible flow solvers [13–17] (especially in the case of marine propellers), and recently either isothermal compressible or fully compressible flow formulations have been used as well [18–21]. If we aim for a precise treatment of hydrodynamic cavitation in its various forms, a compressible multiphase flow model is a requisite for reliable numerical predictions [18]. Peculiarly, the sound speed in a mixture can drop to a fraction of that in the liquid and even the vapor phases. Prediction of the correct acoustic signal speeds calls for a complete flow model.

In this paper, the dynamics of the unsteady sheet cavitation is studied in detail. We employ a compressible two-phase flow model to account for the cavitation phenomena, and the computational case is the ITTC standard cavitator [22]. The results are compared to the model tests carried out in a cavitation tunnel. The flow simulations have been conducted with the general purpose CFD solver FINFLO. The cavitation tunnel tests, which include hydrophone measurements of the underwater noise, have been conducted at SVA Potsdam. We have carried out simulations of two different cases. The inflow velocity for both cases was 8 m/s, and the cavitation numbers were $\sigma = [0.53, 1.27]$. To the knowledge of the authors, our results include the first reported numerical studies of the ITTC standard cavitator.

This paper is organized as follows. Section 2 describes the flow solver used, as well as the turbulence and multiphase flow modelling. In Section 3 we describe the test case. Section 4 presents the results in terms of cavitation observation and its dynamics, and their comparison to the experimental findings. Lastly, we present conclusions and suggestions for future work in Section 5.

2. Flow Solution

2.1. Governing Equations

Our flow model is based on a compressible form of the RANS equations where an assumption is made on the homogeneity of the fluid mixture among the different phases involved in the computation [23,24]. Including the energy equations for the solution allows prediction of the correct acoustic signal speeds. The governing continuity and momentum equations are

$$\begin{aligned} \frac{\partial \alpha_k \rho_k}{\partial t} + \nabla \cdot \alpha_k \rho_k \mathbf{V} &= \Gamma_k, \\ \frac{\partial \rho \mathbf{V}}{\partial t} + \nabla \cdot \rho \mathbf{V}\mathbf{V} + \nabla p &= \nabla \cdot \boldsymbol{\tau}_{ij} + \rho \mathbf{g}, \end{aligned} \tag{1}$$

where p is the pressure, $\mathbf{V}$ the absolute velocity in a global non-rotating coordinate system, $\boldsymbol{\tau}_{ij}$ the stress tensor, α_k a void (volume) fraction of phase k, ρ_k the density, t the time, Γ_k the mass-transfer term, and $\mathbf{g}$ the gravity vector. The void fraction is defined as $\alpha_k = \mathscr{V}_k / \mathscr{V}$, where $\mathscr{V}_k$ denotes the volume occupied by phase k of the total volume, $\mathscr{V}$. For the mass transfer, $\sum_k \Gamma_k = 0$ holds, and consequently

only a single mass-transfer term is needed. The energy equations for phase $k = g$ or l, the indices referring to gas (g) and liquid (l) phases, are written as

$$\frac{\partial \alpha_k \rho_k (e_k + \frac{V^2}{2})}{\partial t} + \nabla \cdot \alpha_k \rho_k (e_k + \frac{V^2}{2}) \mathbf{V} = -\nabla \cdot \alpha_k \mathbf{q}_k + \nabla \cdot \alpha_k \boldsymbol{\tau}_{ij} \cdot \mathbf{V} + q_{ik} + \Gamma_k (h_{k\text{sat}} + \frac{V^2}{2}) + \alpha_k \rho_k \mathbf{g} \cdot \mathbf{V}. \quad (2)$$

Here, e_k is the specific internal energy, $\mathbf{q}_k$ the heat flux, q_{ik} interfacial heat transfer from the interface to phase k, and $h_{k\text{sat}}$ saturation enthalpy. The interfacial heat transfer coefficients are based on the mass-transfer model by assuming a saturated temperature for the gas phase, and the heat transfer is then determined by the mass-transfer model. In the case of a homogeneous flow, the resulting sound speed c for a two-phase mixture is obtained from the eigenvalues of the Jacobian of the flux vector as

$$\frac{1}{\rho c^2} = \frac{\alpha}{\rho_g c_g^2} + \frac{1-\alpha}{\rho_l c_l^2} \quad \text{and} \quad \frac{1}{c_k^2} = \frac{\partial \rho_k}{\partial p} + \frac{1}{\rho_k} \frac{\partial \rho_k}{\partial h_k}. \quad (3)$$

In the expressions above, h_k denotes the enthalpy of phase k.

The momentum and total continuity equations in the homogeneous model do not change, except for the material properties like density and viscosity. They are calculated for the mixture as a weighted sum by the phasic volume fractions. The turbulence effects are those of single-phase models for the mixture with material properties derived from the pressure and temperatures of the individual phases. The determination of the material properties is described in [25].

2.2. Turbulence Modelling

Nominally, a Reynolds-averaged form of the Navier–Stokes equations is used, and the DDES approach [26] that combines RANS and LES is also applied in the same form. In this study, the calculations are performed up to the wall both in the model- and full-scale simulations, which avoids the use of wall functions. The height of the first cell was adjusted such that the non-dimensional wall distance $y^+ = \rho u_\tau y / \mu \lesssim 1$ for the first cell, with $u_\tau = \sqrt{\tau_w / \rho}$ being the friction velocity, τ_w the wall shear stress, and y is the normal distance from the solid surface to the center point of the cell next to the surface.

The base turbulence closure applied in the present calculations is the SST $k - \omega$ model [27]. That is a zonal model, referring to the formulation where the $k - \omega$ equations are solved only inside the boundary layer, and the standard $k - \varepsilon$ equations, transformed to the ω-formulation, are solved away from the walls. The DDES is also based on the SST model [28], and described in [12]. DDES is a slightly modified version of the detached-eddy simulation (DES). Both are hybrid RANS/LES models, and function as an LES subgrid-scale model in regions where the local turbulent phenomena are of greater size than the local grid spacing, and reduce to a RANS model in regions where the largest turbulent fluctuations are of a smaller size than the local grid spacing [29]. A time-accurate solution is made to resolve turbulent fluctuations.

2.3. Mass and Energy Transfer

Several mass-transfer models have been suggested for cavitating problems. Usually, the mass-transfer rate is proportional to a pressure difference from a saturated state or to a square root of that. In this study, we employ a mass-transfer model that is similar to that of Choi and Merkle [30], described in [24,31]. The empirical parameters of the cavitation model are calibrated by Sipilä [3]. The saturation pressure is based on the free-stream temperature, and the gas phase is assumed to be saturated.

2.4. Solution Algorithm

The governing equations are discretized in a finite volume manner with viscous fluxes and pressure terms centrally differenced. For the convective part, a third-order upwind-biased monotonic upstream-centered scheme for conservation laws (MUSCL) interpolation is used for the variables on the cell surfaces. A compressive flux limiter that has been shown to improve the predicted tip vortex cavitation pattern [24] is employed for the void fraction in the present study. For the time derivatives, a second-order three-level fully implicit method is used.

The solution method is a segregated pressure-based algorithm where the momentum equations are solved first, and then a pressure-velocity correction is made. The basic idea in the solution of all equations is that the mass balance is not forced at every iteration cycle, but rather the effect of the mass error is subtracted from the linearized conservation equations. A pressure correction equation was derived from the continuity equation, Equation (1), linked with the linearized momentum equation. The velocity-pressure coupling is based on the corresponding algorithm for a single-phase flow [23], and is described in more detail in [12,24]. A physical time step of $\Delta t = 2.5 \times 10^{-5}$ s is used in the simulations, which resolves the cavitation dynamics cycles in the investigated cases with about 250 ($\sigma = 1.27$) and 1200 ($\sigma = 0.53$) steps depending on the conditions. Approximately 100 inner iterations were required within each physical time step.

3. Test Case

A schematic view of the ITTC standard cavitator is shown in Figure 2, and the cavitator inside the cavitation tunnel is seen in Figure 3. The rectangular cross-section of the tunnel has the dimensions of 600×600 mm^2. Two cases with different cavitation numbers were investigated. The inflow velocity for both cases was $U_\infty = 8$ m/s, and the cavitation numbers were

$$\sigma = \frac{p - p_{sat}}{\frac{1}{2}\rho_\infty U_\infty^2} = [0.53, 1.27] \, .$$

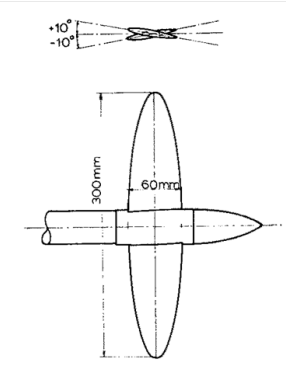

Figure 2. Schematic view of the cavitator.

Three grid densities were used in the calculations. The details are summarized in Table 1. The structured grid has an O-O topology around the foils. The finest grid level consists of roughly 7.3 million cells in 80 grid blocks. The grid resolution around the leading and trailing edges is reasonable, and there are about 15 cells around the leading-edge radius. Due to the O-O topology, the same resolution is applied around the blade tip and the trailing edge as well. In this work, we emphasized the resolution of the sheet cavitation on the wings, and for this reason no clustering of cells was targeted for the cavitating tip vortex, for instance. The grid is refined normal to the viscous surfaces such that $y^+ \approx 1$ at the finest grid level. A detail of the grid is shown in Figure 4, and the grid resolution on the surface of the foil is shown in Figure 5.

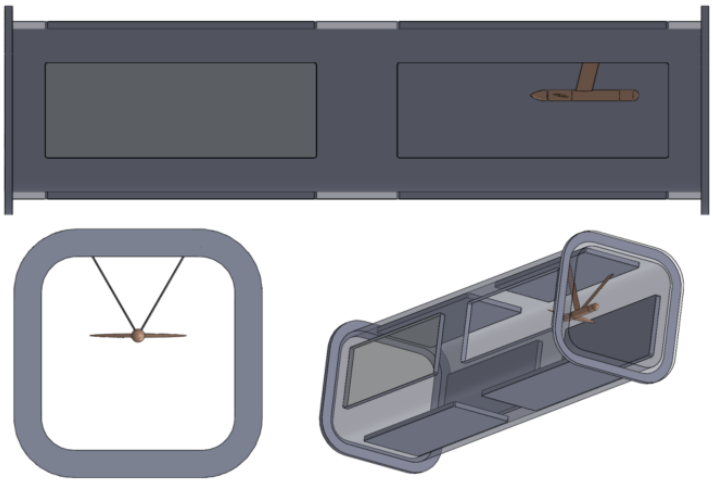

Figure 3. Placement of the cavitator inside the cavitation tunnel.

Table 1. Summary of the details of the grid used in the calculations for the three grid levels. The number of surface cells are given for one side of the foil.

	Fine Grid	Medium Grid	Coarse Grid
Total number of cells	7,254,528	906,816	113,352
Surface cells in chordwise direction	96	48	24
Surface cells in spanwise direction	96	48	24

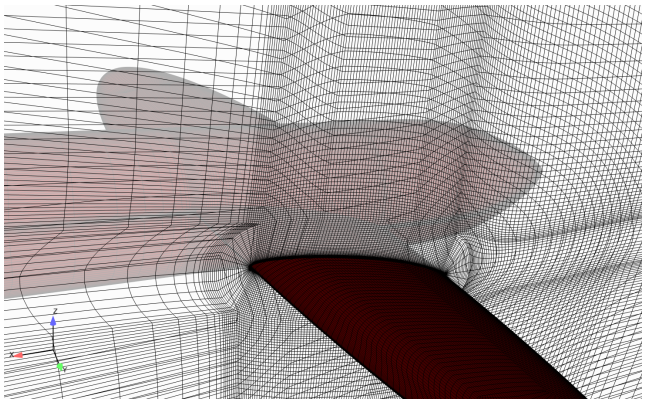

Figure 4. A detail of the grid near the foil.

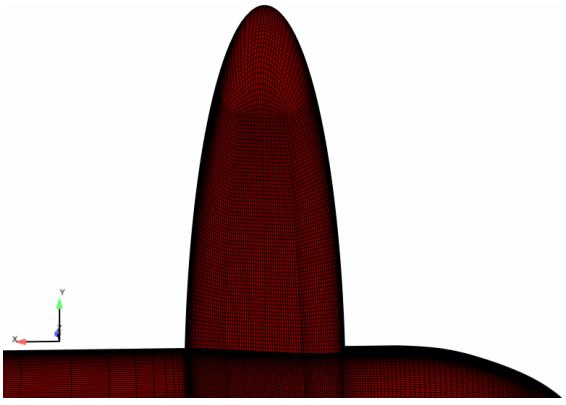

Figure 5. Grid resolution on the surface of the foil. Fine grid.

The foils and the body are modelled as no-slip solid surfaces. A velocity boundary condition is applied at the inlet, and a pressure boundary condition is applied at the outlet. Slip boundary condition is applied at the tunnel walls. The inflow velocity is set based on the case considered, and the background pressure level is set to either a large value for the wetted flow simulations, $\mathcal{O}(10^6)$, or set based on the cavitation numbers in the cavitating cases. The calculations can be typically performed on three grid levels. On the coarser grid levels, every second point is taken into account compared to the finer level grid. The computations on a coarser grid are used as the initial guess for the computations performed on a finer grid. Initially, we made the unsteady computations for the coarse and medium size meshes to keep the computational time within reasonable limits. However, for the $\sigma = 1.27$ case, the cavitation extent is not as wide as in the $\sigma = 0.53$ case, and the dynamics appear at a higher frequency. To capture better cavitation dynamics, we considered it adequate to also use a finer mesh in the simulations.

4. Results

4.1. Cavitation Observation

Cavitation observations made in the experiments in the case with $U_\infty = 8$ m/s and $\sigma = 0.53$ are shown in Figure 6, and a snapshot of the simulations with the SST model is given in Figure 7, where the pressure coefficient is defined as $C_p = 2p_{dif}/\rho_\infty U_\infty^2$, where p_{dif} denotes the pressure difference. Generally, attached sheet cavitation covers roughly half of the suction side in the experiments with cavitation incepting at the leading edge. Almost the entire suction side is covered by unstable detached sheet cavitation in the simulations. Strong and periodic shedding of the sheet cavitation are observed in the simulations, with cloud-like cavities shedding to the wake of the foils. In the experiments, the sheet cavitation is observed to break off as cloud cavitation. We observed streak cavitation at the hemispherical head of the cavitator body in the experiments.

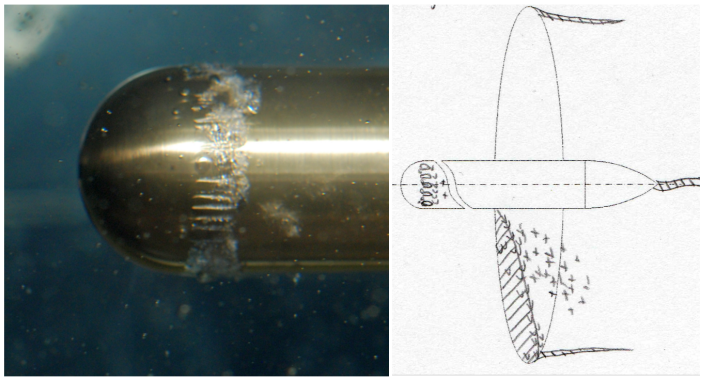

Figure 6. Cavitation extent observed in the experiments with $U_\infty = 8$ m/s and $\sigma = 0.53$. Left picture shows a photograph of the head of the cavitator in the experiments, and right picture shows a sketch of the mean cavitation extent on the cavitator. The pictures are reproduced with permission from Rhena Klose (SVA).

In the simulations, however, we see attached sheet cavitation at the hemispherical head of the cavitator body. Strong hub vortex cavitation extending far behind the cavitator body is also observed both in the experiments as well as in the simulations. We notice that in the experiments, a fine tip vortex cavitation extends roughly a chord length in the slipstream, while in the simulations tip vortex cavitation is not visible. In the simulations, strong disturbances created by the unsteady suction side sheet cavities are observed both in the pressure coefficient as well as in the non-dimensional v-velocity. In particular, a collapse event of a cavity cloud gave rise to a considerable pressure peak and a subsequent shock-wave-like front in the wake of the foil. The disturbances in C_p and v-velocity, however, dissipate quickly near the end of the cavitator body as the grid resolution deteriorates.

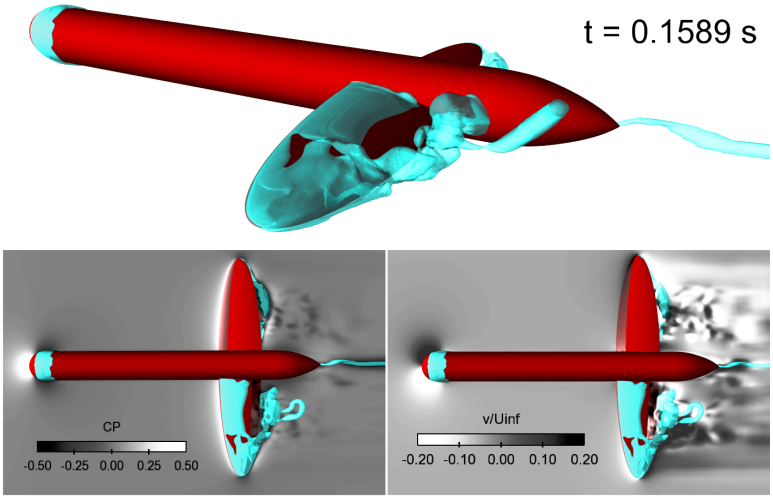

Figure 7. A snapshot of the simulations with $U_\infty = 8$ m/s and $\sigma = 0.53$. Fine grid with the SST turbulence model. Top frame presents an overview of the cavity extent with the transparent iso-surface of $\alpha = 0.1$ colored by blue. Lower left frame shows the pressure coefficient on the center z plane of the cavitator. Lower right frame shows the non-dimensional v-velocity on the center z plane of the cavitator.

Cavitation observations made in the experiments in the case with $U_\infty = 8$ m/s and $\sigma = 1.27$ are shown in Figure 8, and a snapshot of the DDES is shown in Figure 9. Generally, sheet cavitation covers roughly half of the suction side in the experiments, and roughly one third of the suction side in the simulations with cavitation incepting at the leading edge. Periodic shedding of the sheet cavitation into smaller cavity structures is observed in the simulations. These smaller cavities convected a distance along the foil before disappearing. In the experiments, parts of the sheet cavitation are observed to break off as cloud cavitation. A cavitating hub vortex is visible both in the experiments as well as in the simulations. We noticed that in the experiments, a very fine tip vortex cavitation extends roughly a chord length in the slipstream, while in the simulations tip vortex cavitation is not visible. In the simulations, disturbances created by the unsteady suction side sheet cavities are observed both in the pressure coefficient as well as in the non-dimensional v-velocity. A collapse event of the smaller cavity structures gave rise to a pressure peak and a subsequent shock-wave-like front in the wake of the foil. The disturbances, however, dissipate quickly near the end of the cavitator body as the grid resolution deteriorates.

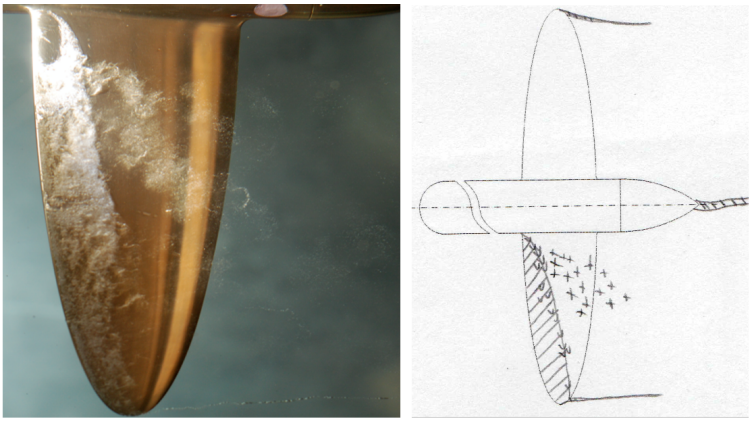

Figure 8. Cavitation extent observed in the experiments with $U_\infty = 8$ m/s and $\sigma = 1.27$. Left picture shows a photograph of the right foil of the cavitator in the experiments, and right picture shows a sketch of the mean cavitation extent on the cavitator. The pictures are reproduced with permission from Rhena Klose (SVA).

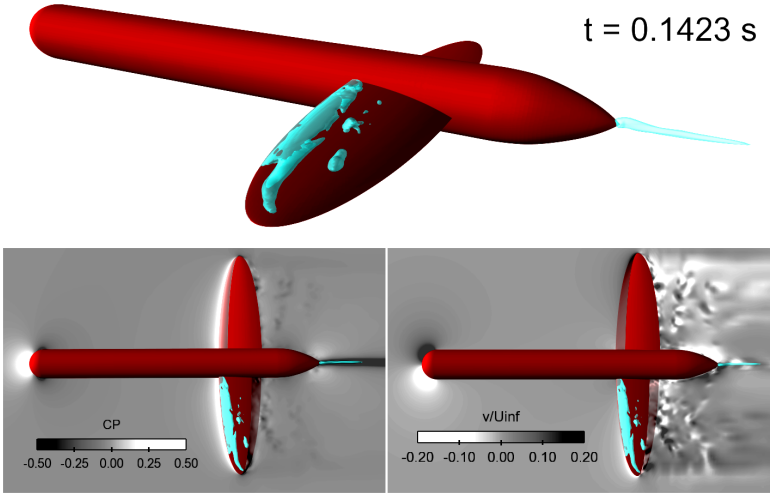

Figure 9. A snapshot of the simulations with $U_\infty = 8$ m/s and $\sigma = 1.27$. Fine grid DDES. Top frame presents an overview of the cavity extent with the transparent iso-surface of $\alpha = 0.1$ colored by blue. Lower left frame shows the pressure coefficient on the center z plane of the cavitator. Lower right frame shows the non-dimensional v-velocity on the center z plane of the cavitator.

4.2. Global Forces

The mean values of the lift and drag coefficients were extracted from the simulations. In addition, we carried out a Fourier analysis for the lift and drag forces on the wings to determine the unsteady characteristics of especially the sheet-cavitation shedding. The results are shown in Table 2 for all investigated cases.

Table 2. Comparison of the mean lift and drag coefficients ($C_{\mathscr{L}}$ and $C_{\mathscr{D}}$, respectively), and their dominant frequencies (f_0).

Case	$\overline{C}_{\mathscr{L}}$	$\overline{C}_{\mathscr{D}}$	Lift: f_0 (Hz)	Drag: f_0 (Hz)
$U_\infty = 8.0$ m/s, $\sigma = 0.53$				
Left foil: coarse grid, SST	0.078	0.025	29.0	29.0
Right foil: coarse grid, SST	0.078	0.025	29.0	29.0
Left foil: coarse grid, DDES	0.079	0.025	29.0	29.0
Right foil: coarse grid, DDES	0.079	0.025	29.0	29.0
Left foil: medium grid, SST	0.071	0.023	29.0	29.0
Right foil: medium grid, SST	0.071	0.023	29.0	29.0
Left foil: medium grid, DDES	0.075	0.024	33.4	35.0
Right foil: medium grid, DDES	0.075	0.024	33.4	35.0
$U_\infty = 8.0$ m/s, $\sigma = 1.27$				
Left foil: coarse grid, DDES	0.110	0.019	-	-
Right foil: coarse grid, DDES	0.109	0.019	-	-
Left foil: medium grid, DDES	0.121	0.017	160.2	160.2
Right foil: medium grid, DDES	0.120	0.017	160.2	160.2
Left foil: fine grid, DDES	0.118	0.016	159.6	159.9
Right foil: fine grid, DDES	0.117	0.016	159.8	160.2

We observed a dominant frequency of around 30 Hz for the case with and $\sigma = 0.53$. We show an example of the time histories and corresponding frequency contents in Figure 10 obtained from DDES, and in Figure 11 obtained from the SST simulations. A frequency of 29.0 Hz for both the lift and drag coefficients was seen with coarse and medium grids when using the SST model. A dominant frequency of 29.0 Hz was observed with coarse grid DDES for both the lift and drag coefficients, while a dominant frequency of 33.4 Hz was observed for lift and 35.0 Hz was observed for the drag with medium grid DDES. Animations from fine and medium grid DDES and SST simulations

revealed a frequency of approximately 30 Hz for the sheet-cavitation shedding. Comparing the DDES and SST simulations, we see that the shedding frequency increases slightly with DDES on the medium grid. The time histories of the SST simulations appear slightly more regular, which is seen also as the sharper frequency peaks whereas these are more spread when using DDES. If we approximate the reference length of the Strouhal number as the chord length, the Strouhal numbers' range is $St = fc/U_\infty = [0.22 \ldots 0.26]$. If we instead take the reference velocity as $U_{ref} = U_\infty\sqrt{1+\sigma}$, the Strouhal numbers would range as $St = [0.18 \ldots 0.21]$.

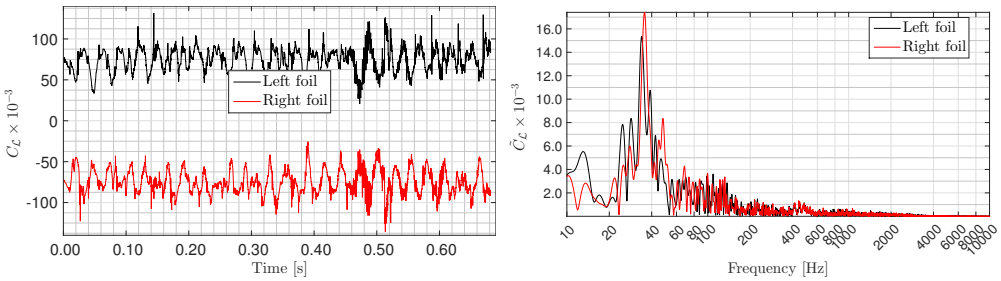

(**a**) Time history of lift coefficient (**b**) Frequency content of lift coefficient

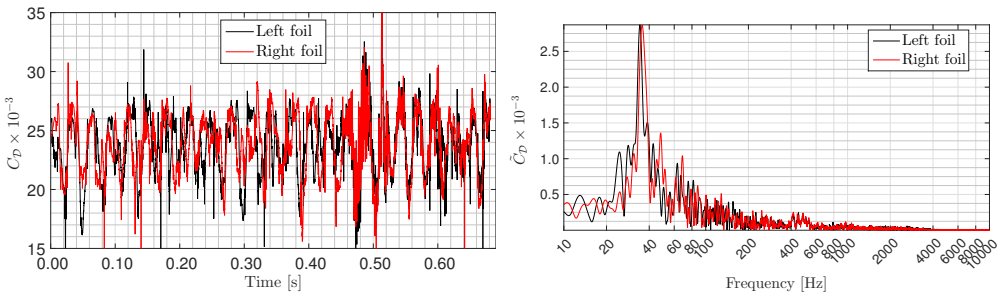

(**c**) Time history of drag coefficient (**d**) Frequency content of drag coefficient

Figure 10. Time history and frequency content of the lift and drag coefficients. Medium grid, $\sigma = 0.53$, DDES.

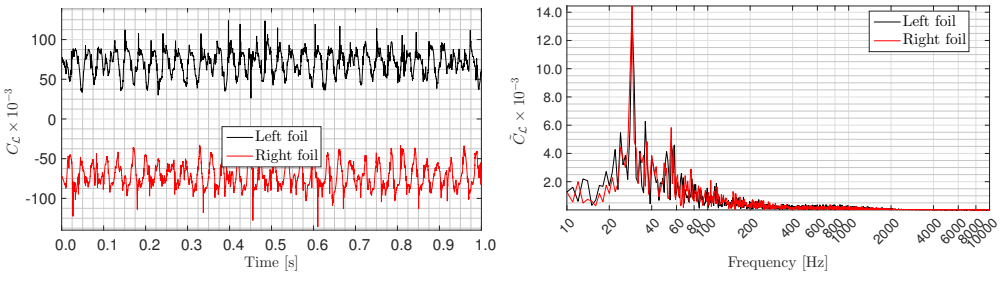

(**a**) Time history of lift coefficient (**b**) Frequency content of lift coefficient

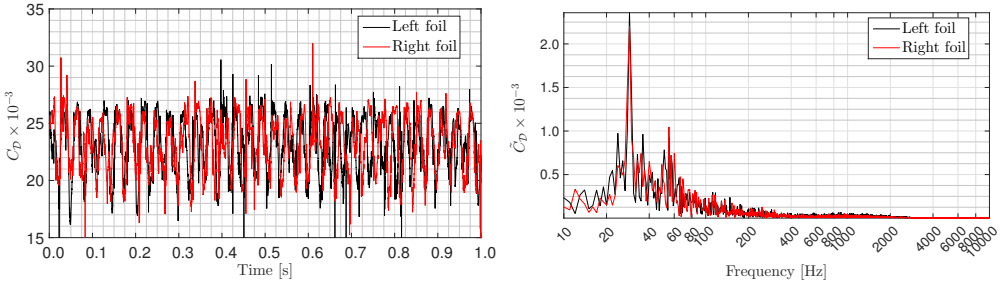

(**c**) Time history of drag coefficient (**d**) Frequency content of drag coefficient

Figure 11. Time history and frequency content of the lift and drag coefficients. Medium grid, $\sigma = 0.53$, SST simulations.

For the case with $\sigma = 1.27$ a dominant frequency in between 159.6–160.2 Hz for both the lift and drag coefficients was observed with medium and fine grid DDES. As we discuss later in Section 4.6, the SST model yielded a steady-state solution for this case. The time histories and corresponding frequency contents are shown in Figure 12. Also, the animations created from fine and medium grid DDES revealed a frequency of approximately 160 Hz for the sheet-cavitation shedding. If we approximate the reference length of the Strouhal number as a quarter of the chord length, the Strouhal number would be $St = fc/U_\infty = 0.30$. If instead we take the reference velocity as $U_{ref} = U_\infty\sqrt{1+\sigma}$, the Strouhal number would be $St = 0.20$. Compared to the case with the lower cavitation number, we now see more distinct peaks even up to the 4th harmonics of the lift and drag.

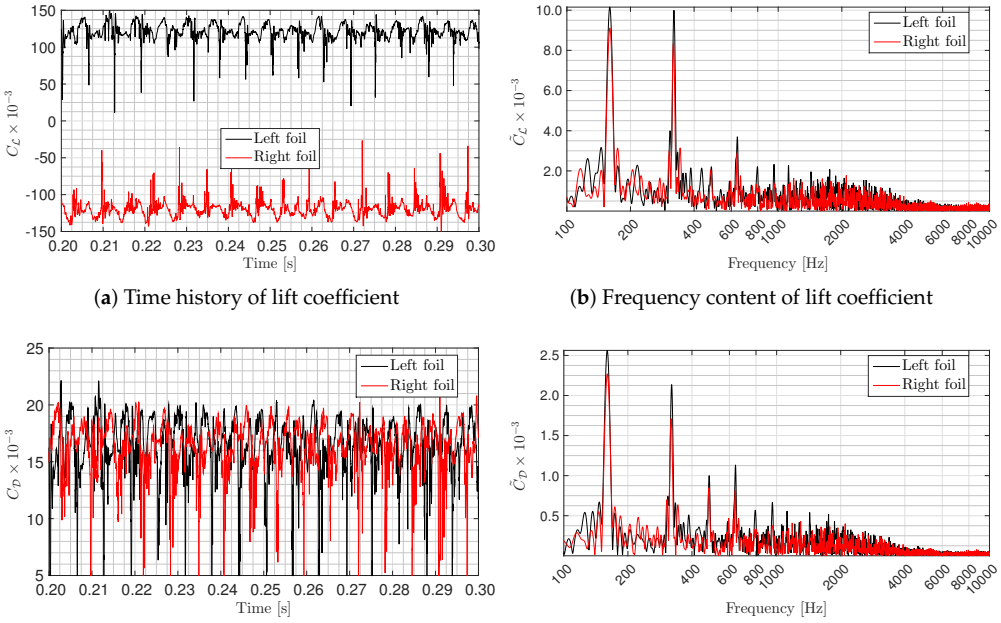

(**a**) Time history of lift coefficient

(**b**) Frequency content of lift coefficient

(**c**) Time history of drag coefficient

(**d**) Frequency content of drag coefficient

Figure 12. Time history and frequency content of the lift and drag coefficients. Fine grid, $\sigma = 1.27$, DDES.

We note that the conducted simulation time was not enough with the fine grid for the case with $\sigma = 0.53$ to provide a sufficient time history to conduct a reliable Fourier analysis. The resolution on the coarse grid was not enough to obtain a reasonable frequency for the cavitation shedding with $\sigma = 1.27$.

There was a small deviation between the mean lift coefficients of the left and right foils with the same cavitation number, while the mean drag coefficients were the same for both foils on each grid. We noted small differences also in the frequencies exhibited in the time histories. A decrease of approximately 40% of the mean lift and an increase of approximately 40% of the mean drag are seen in the results with $\sigma = 0.53$ compared to the results of $\sigma = 1.27$. This is because there is considerably more suction side sheet cavitation for the case with $\sigma = 0.53$, since the cavitation number is lower. The increase in the amount of the vapor phase on the suction side in turn decreased the lift and increased the drag of the foil. This difference was visible in the results using each of the three different grid densities.

4.3. Analyses of Cavitation Dynamics

Next, we compare the simulations to the experiments in Section 4.3.1 in terms of the hydrophone measurements. The dynamics of the investigated cases with different cavitation numbers are then analyzed in Sections 4.3.3 and 4.3.4. Cavitation collapse events and resulting pressure variations are investigated in Section 4.4. Later in Section 4.5 we demonstrate a formation of a cavitating ring vortex, and in Section 4.6 a comparison of the DDES and SST simulations is shown.

4.3.1. Comparisons with Hydrophone Measurements

Different hydrophone configurations were tested in the cavitation tunnel of SVA Potsdam, depicted in Figure 13 and summarized in Table 3. The hydrophones were installed on the starboard side of the cavitation tunnel window.

Table 3. Hydrophone arrangements in the cavitation tunnel.

Hydrophone	Installation
HF1	Upstream, acoustic chamber
HF2	Downstream, acoustic chamber
HF3	Upstream, longitudinally to the flow
HF4	Downstream, longitudinally to the flow
HF5	Upstream, transversal to the flow
HF6	Downstream, transversal to the flow

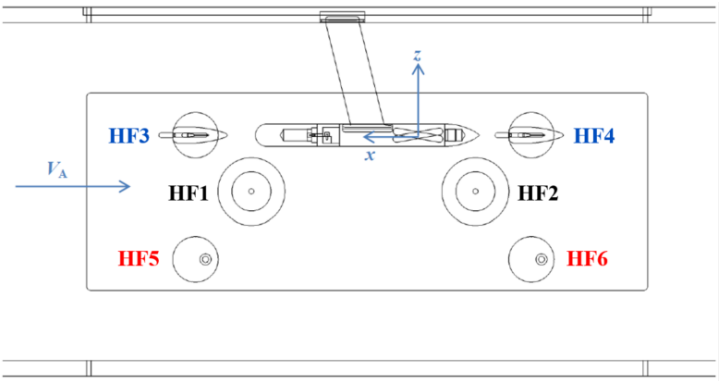

Figure 13. Hydrophone arrangement in the starboard side of the cavitation tunnel. Figure adapted from [32], and reproduced with permission from Rhena Klose (SVA).

Figure 14 shows the results of the conducted hydrophone measurements. In the figures, we show six different hydrophone arrangements. HF1 and HF2 denote the hydrophones in an acoustic chamber, with HF1 mounted in the wall of the cavitation tunnel at a distance of 0.500 m from the origin of the cavitator (see Figure 13), and HF2 mounted a distance of 0.414 m from the cavitator. HF3 and HF4 are located longitudinally to the flow, and the distances to the cavitator are 0.543 m for HF3 m and 0.352 m for HF4. HF5 and HF6 are located transversally to the flow, and the distances to the cavitator are 0.522 m for HF5 m and 0.420 m for HF6. The sensors HF1, HF3 and HF5 are located upstream of the cavitator, and the sensors HF2, HF4 and HF6 are located downstream of the cavitator.

Figure 14a shows the case with $\sigma = 0.53$, and Figure 14b shows the case with $\sigma = 1.27$. In both instances, the predicted sheet-cavitation shedding frequencies and their three harmonics are shown as well, cf. Section 4.2. We observe that in the case of $\sigma = 0.53$, the shedding frequency is picked up by hydrophones HF1, HF2, HF3 and HF4. Moreover, the measurements conducted with HF2, HF3 and HF4 show a smaller peak at the second harmonic of the sheet-cavitation shedding frequency. In the case of $\sigma = 1.27$, we see that the CFD predicted cavitation shedding frequency peak is visible only in the HF1 measurements. Other frequencies are also seen in the hydrophone measurements that are of greater magnitude than the ones induced by cavitation dynamics in the CFD simulations.

For instance, the shedding cavities formed into cloud-like cavitation structures both in the experiments as well as in the simulations, in both the investigated operation points. This should manifest itself as a high-frequency source of noise, the type of which is seen in the hydrophone signals in Figure 14: at frequencies between approximately 100 Hz and 1 kHz for the case with $\sigma = 0.53$ and at frequencies around 1–2 kHz for $\sigma = 1.27$, visible especially in the hydrophones HF1 and HF2. The high-frequency broadband noise is likely due in part to very rapid collapse events of the cavity clouds once they reach a region of sufficiently high pressure in the slipstream of the cavitator. A cavitation collapse event is assessed in Section 4.4. The best arrangement of hydrophones in the tests for the investigations with the standard cavitator turned out to be the one in the acoustic chamber, i.e., hydrophones HF1 and HF2.

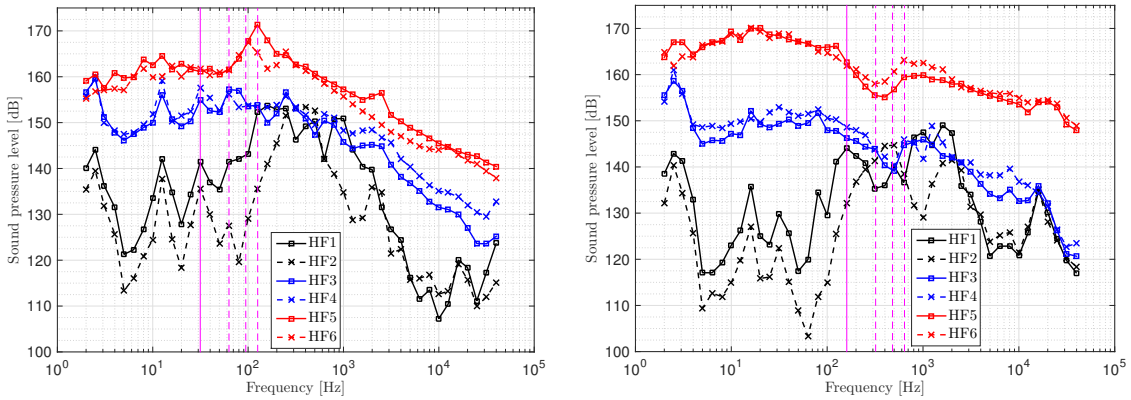

(**a**) $\sigma = 0.53$ (**b**) $\sigma = 1.27$

Figure 14. Sound pressure level measurements inside the cavitation tunnel with different hydrophone arrangements. The magenta vertical lines denote the predicted cavitation shedding frequency and its harmonics. The measurement results were reproduced with permission from Rhena Klose (SVA).

4.3.2. Cavitation Dynamics and Shedding Mechanisms

Below in Sections 4.3.3 and 4.3.4, we discuss observations of the sheet-cavitation dynamics and shedding mechanisms. Figure 15 shows a sheet-cavitation shedding cycle of the case with $\sigma = 0.53$. Figure 16 shows a sheet-cavitation shedding cycle of the case with $\sigma = 1.27$. Former The results are obtained for the former on the medium grid, and the latter on the fine grid. We study here the cavitation dynamics by visualizing on the left side of a frame the rate of evaporation together with velocity vectors on a cut plane at mid-span, as well as the contour of void fraction value $\alpha = 0.1$. A negative rate of evaporation denotes the rate of condensation. Additionally, on the right side of the frame a perspective view of the cavitation extent is shown by an iso-surface of $\alpha = 0.1$. In each figure, six frames are presented to represent one cavitation shedding cycle. The shedding cycle is taken as the corresponding frequency shown earlier in Table 2. It is notable that the flow features and cavitation dynamics, especially in the case with the lower cavitation number, were observed as highly three-dimensional over the span of the foil. Nevertheless, we focus on a qualitative sense on the flow features of the aforementioned cut plane at mid-span.

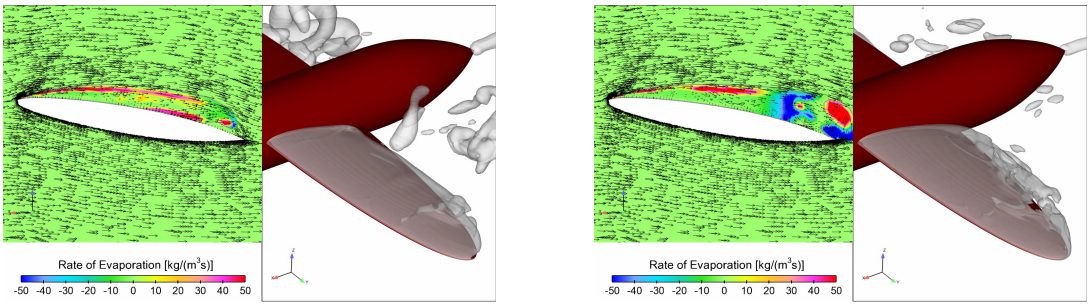

Frame 1. Frame 2.

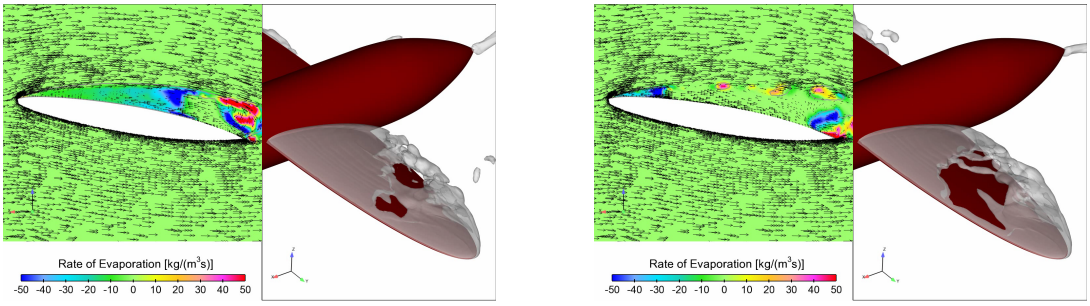

Frame 3. Frame 4.

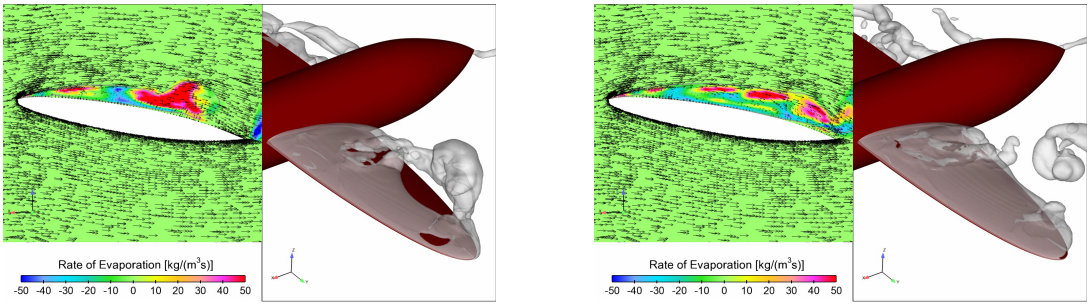

Frame 5. Frame 6.

Figure 15. A sequence of snapshots visualizing one suction side sheet-cavitation shedding cycle. DDES on medium grid, $\sigma = 0.53$. Left frame depicts a cut plane of the left foil at mid-span, with velocity vectors denoted by arrows (only 25% of the velocity vectors is drawn on the plane for clarity), contour of the void fraction $\alpha = 0.1$ denoted by the grey curves, and the plane is colored by the rate of evaporation. The right frame shows the cavity extent near the left foil by an iso-surface of $\alpha = 0.1$. The frame number denotes the respective stage of the cycle.

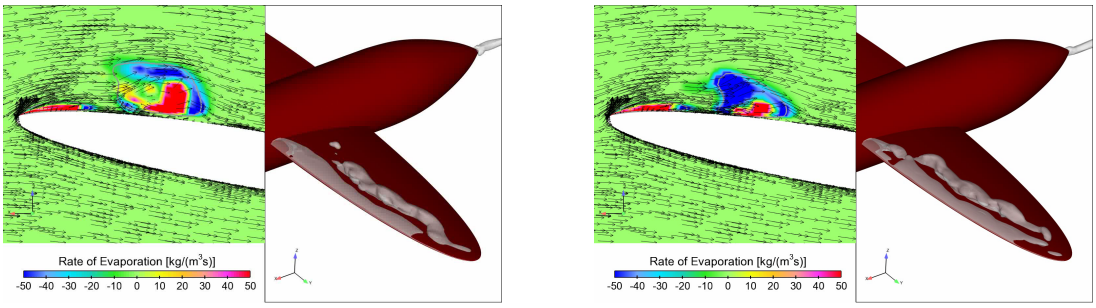

Frame 1. Frame 2.

Figure 16. *Cont.*

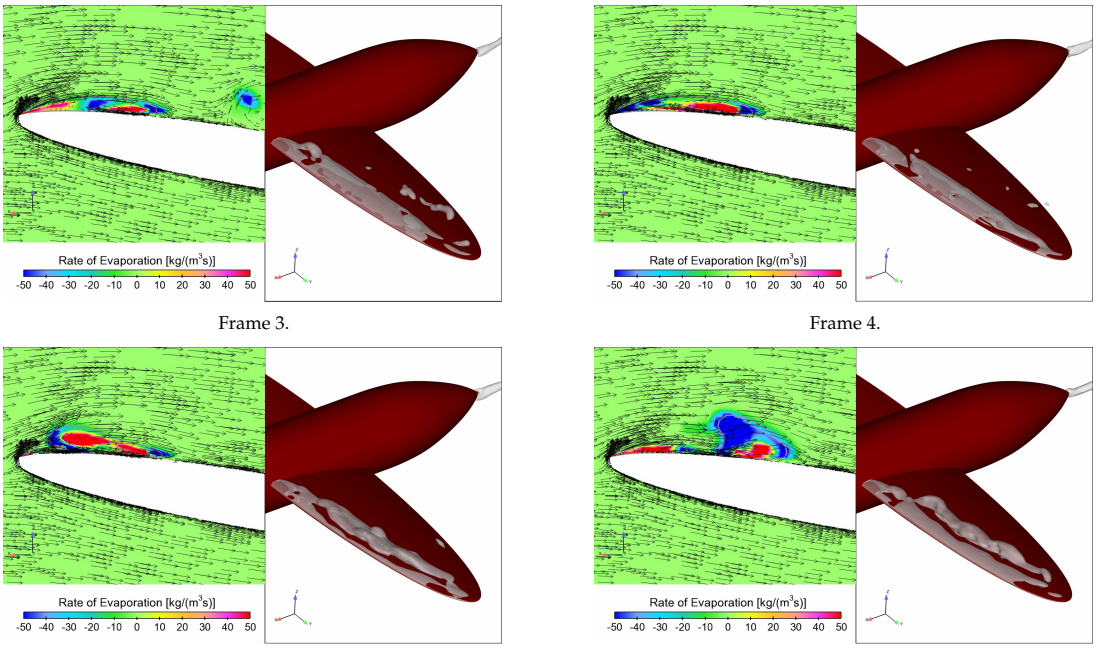

Figure 16. A sequence of snapshots visualizing one suction side sheet-cavitation shedding cycle. Fine grid, $\sigma = 1.27$, DDES. Left frame depicts a cut plane of the left foil at mid-span, with velocity vectors denoted by arrows (only 25% of the velocity vectors is drawn on the plane for clarity), contour of the void fraction $\alpha = 0.1$ denoted by the grey curves, and the plane is colored by the rate of evaporation. The right frame shows the cavity extent near the left foil by an iso-surface of $\alpha = 0.1$. The frame number denotes the respective stage of the cycle.

4.3.3. Cavitation Dynamics: $\sigma = 0.53$

In the first frame of Figure 15 (case $\sigma = 0.53$) a cavity cloud is shed in the wake of the foil, and an attached sheet cavity has grown from the leading edge of the foil. There is strong evaporation in the layers close to the wall of the sheet cavity and on the upper surface of the cavity. Some condensation takes place at the closure of the sheet cavity. Parts of the shed cavity clouds convect still farther downstream, visible in the right side of the first frame. The frames 1–2 depict the growth of the attached sheet cavitation to super-cavitation, where the sheet cavity momentarily covers the entire suction side of the foil. A re-entrant jet is observed at the closure line of the sheet cavitation in frame 2. Once we reach Frame 3, the re-entrant jet has impinged the sheet cavitation, and continues to a draw liquid phase underneath it. We also notice strengthening condensation at the closure of the sheet cavitation in frames 2–3, as well as strong vorticity as the shedding initiates. By Frame 4, almost all sheet cavity has detached at mid-span, and the re-entrant jet has further intensified. We observe that the impingement does not occur simultaneously over the whole span, but rather exhibits a highly three-dimensional shape and structure with the root and tip parts of the foil still completely covered by the sheet cavitation. As we reach Frame 5, a large cavity cloud is broken off the sheet cavity, which is convected to the wake of the foil. Strong evaporation begins again on the foil as we notice at the cut plane. Finally, once we reach Frame 6 the sheet cavitation at the LE continues to grow, and the broken-off cavity clouds are convected farther in the wake by the external flow over the foil. A new shedding cycle is then initiated at Frame 6. Again we note that while the visually observed shedding cycle was confirmed by the dominant frequencies of the lift and drag coefficients, the two-phase flow over the span is three-dimensional and, for instance, separate and phase-lagging breaking cycles were observed near the root parts of the foil.

4.3.4. Cavitation Dynamics: $\sigma = 1.27$

Similarly as above, the first frame of Figure 16 (case $\sigma = 1.27$) depicts the initial stages the attached sheet cavity growth. Cavity clouds are shed in the wake of the foil, and an attached sheet cavity begins to grow from the leading edge of the foil. There is strong evaporation in the layers close to the wall of the sheet cavity, and condensation takes place on the closure of the forming cavity. A detached cavity cloud is convected to the slipstream and vortical flow is associated with it. In frames 2–3, the attached sheet cavitation grows in length along the foil. In Frame 2, we observe evaporation at the center of the attached cavity cloud, whereas condensation takes place around the closure of the sheet cavity. As we reach Frame 3 a re-entrant jet is visible. The jet draws the liquid phase toward the LE, underneath the sheet cavity and splits the evaporation zone of the previous frame in two parts. Frame 4 depicts a partial break-off stage as the re-entrant jet begins to impinge the sheet cavity. Condensation now takes place both in the LE and the TE of the detaching cavity, although evaporation is present at its core. A tiny cavity at the LE of the foil begins to form. Once we reach Frame 5, the impingement of the re-entrant jet is more complete, and we observe that the sheet cavity has broken off on a wide span. The cavity cloud starts to rise away from the foil to be convected by the external flow. Stronger vortical flow forms around the core of the detached cavity. In Frame 6 we observe this cavity cloud being convected farther in the wake, as a new shedding cycle is about to begin. We furthermore observe condensation beginning to dominate over evaporation in the detached cavity. A strong recirculating flow is visible around the detached cavity cloud. Again, the flow is three-dimensional over the span of the foil, and the break-off does not occur simultaneously over the span.

4.4. Cavitation Collapse Events and Pressure Waves

In Figure 17 we show a set of snapshots for a stage of the shedding cycle at which the cavity undergoes a rapid collapsing stage, and the associated instantaneous pressure distributions. The figure shows the case with the lower cavitation number, $\sigma = 0.53$. The cavity cloud has shed off at t_0, and we observe an increase in pressure on the plane at mid-span, just below the cavity. As the collapse stage advances, the pressure values grow larger, and the pressure front starts to propagate in all directions quite rapidly. We note very high values for the C_p due to the major collapse events $t_0 + 0.8$ ms. The maximum value recorded for the investigated plane was $\approx$3. After this, the pressure wave front grows and intensifies, and then also quickly dissipates. Next, we are left with small regions of negative pressure in the place of the shed cavity clouds at the two latest investigated time instants. Looking at the cavitator body, the pressure wave due to the major collapse at $t_0 + 0.8$ ms reaches it a few tenths of ms later. The cavitator body on the upstream side of the wing shows areas of increased positive pressure, and the downstream side of it in turn has a momentarily lower negative pressure. At the moment of the collapse event, also high pressures are recorded on the suction side of the wing near the trailing edge, as the cavity collapses just above it, at the same time the pressure side of the wing is masked from this effect. The dynamics of the bulk cavitation on the wing, then again, appears to be unaffected by the pressure waves that result from the cavity collapse. The attached sheet cavitation continues to grow on to enter the shedding phase described in Section 4.3.3. Also, at subsequent time instants, the shed-off cavity continues to form the cavitating ring vortex. We assess this further in Section 4.5. The cavitating vortex due to the hub of the cavitator body also appears to be not affected by the collapse event.

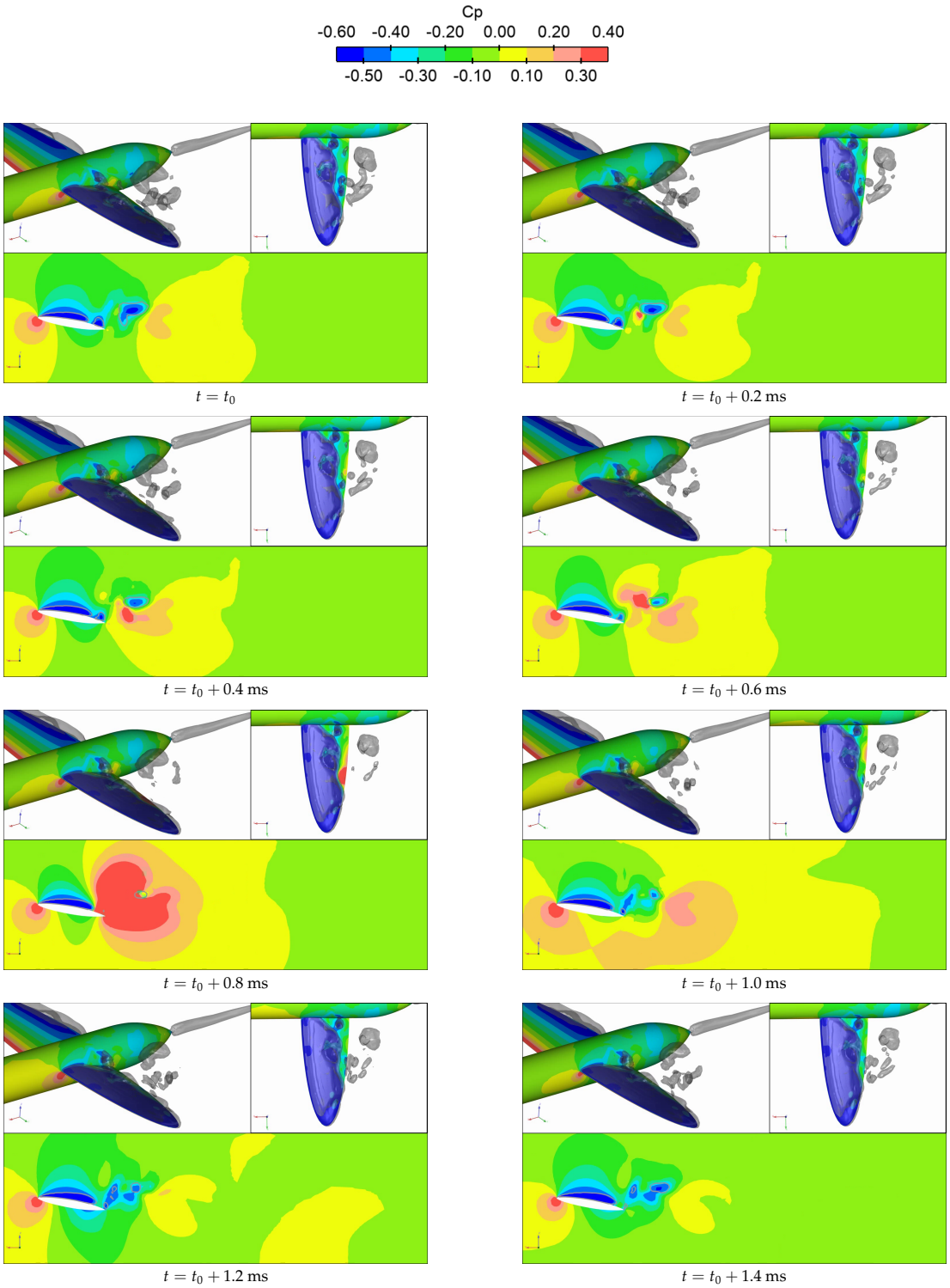

Figure 17. A sequence of snapshots visualizing a collapse event of the cavity. DDES with medium grid, $\sigma = 0.53$. Top frames show the left wing from the side and the top, and the bottom frame shows a cut plane at mid-span. The cavitator and the cut plane are colored by C_p.

4.5. A Formation of Cavitating Ring Vortex

In Figure 18 we demonstrate the formation of a cavitating ring vortex. The figure depicts six snapshots at 2 ms intervals of the DDES on a medium grid with $U_\infty = 8$ m/s and $\sigma = 0.53$. On the left side of each frame, the isosurfaces of $\alpha = 0.1$ and Q = 40,000 are shown. Moreover, the Q-criterion is colored by helicity $\mathrm{H} = u_i\Omega_i/(|u_i||\Omega_i|)$. The helicity denotes the cosine of the angle between the velocity and the vorticity vectors, and tends to ± 1 in the cores of free vortices, the sign indicating the direction of swirl. On the right side of each frame, three cut planes are shown at spans of $y/s = [0.25, 0.50, 0.75]$, which are colored by the rate of evaporation R. Also, on the right side of each frame, the iso-surface of $\alpha = 0.1$ is shown as the transparent orange surface. At the beginning of this series of snapshots ($t = t_0$), we are approaching the end of a shedding cycle (cf. Figure 15) with cavitation and vortical flow structures being shed in the wake of the foil. A complex interaction with the shedding vapor clouds and liquid-phase flow introduce vast vortical flow structures when the sheet cavity detachment takes place between $t = t_0$ and 2 ms. As separate and partially cavitating vortex filaments convect downstream, some of these join together to form a ring-shaped structure, or a toroidal-type vortex between $t = t_0 + 2$ and $\ldots 6$ ms. Observing the helicity of these toroids, we note that once it is a true vortex ring or even a piece of such, the vorticity is strong enough for the flow inside these rings to cavitate in most parts clearer and at a higher intensity. Once these structures convect farther downstream ($t = t_0 + 8 \ldots 10$ ms), dissipation owing to the coarsening grid in the wake diminishes the strength of the toroid-like shape, leading to dissipation of the cavitation as well, despite the used compressive flux limiter. Moreover, as was mentioned above, we observe the strongly three-dimensional cavitation structure in Figure 18. For instance, the rates of evaporation on the three cut planes are vastly different from each other, albeit the sheet cavitation covering the entire foil superficially appears as rather steady at several time instants. Also chord- and spanwise fluctuations can be observed on the iso-surface of the Q-criterion.

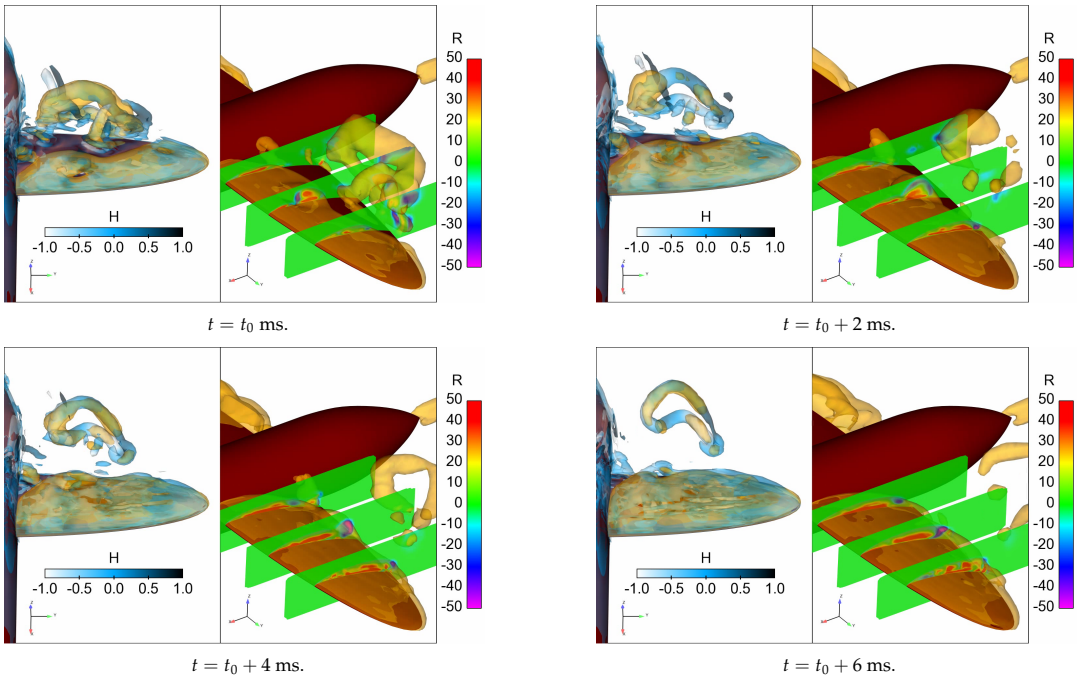

$t = t_0$ ms. $t = t_0 + 2$ ms.

$t = t_0 + 4$ ms. $t = t_0 + 6$ ms.

Figure 18. *Cont.*

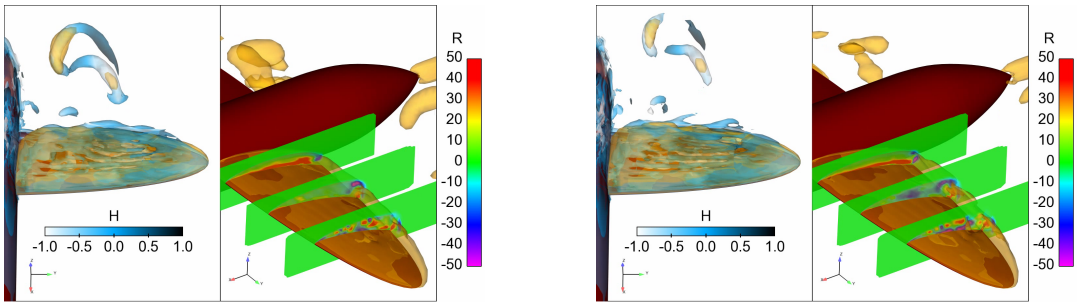

$t = t_0 + 8$ ms. $t = t_0 + 10$ ms.

Figure 18. A sequence of snapshots depicting the formation of a partial cavitating ring vortex in the wake of the foil. DDES with medium grid, $\sigma = 0.53$. On the left in each frame: left foil with iso-surface of void fraction $\alpha = 0.1$ colored as orange, together with an iso-surface of $Q = 40,000$, which is colored by the helicity H. On the right in each frame: three cut planes at $y/s = [0.25, 0.50, 0.75]$ which are colored by the rate of evaporation R, with iso-surface of void fraction $\alpha = 0.1$ colored as orange.

4.6. A Comparison of Different Turbulence Closures

A peculiar modelling issue regarding the cavitation dynamics was observed during the simulations. The case with $\sigma = 1.27$ was initially begun with the SST model, but the predicted suction side sheet cavitation remained stable throughout the simulations. We observed no natural shedding of the sheet cavitation, and the time histories of the global forces were flat. We carried out the simulations with the SST model until $t \approx 0.155$ s, after which the DDES approach was activated. The outcome is illustrated in Figure 19 in terms of the time histories of the lift and drag coefficients. It was observed that almost immediately after the DDES approach was activated, the suction side sheet cavitation began its shedding behavior, leading to high-frequency oscillations also in the global force coefficients.

A comparison of the DDES and the SST simulation is shown in Figure 20, made from visualizations of the eddy-viscosity levels near the LE of the foil on a cut plane at mid-span, cavitation extents and vortical flow structures. We observe a significant difference in the eddy-viscosity distributions. The SST simulation predicts several orders of magnitude larger eddy-viscosity levels on the suction side of the foil. This not only suppresses any vortical structures around the foil, but also prevents the natural shedding mechanisms of the sheet cavitation to take place. Instead, the predicted suction side cavitation remained stable as consequently did the lift and drag forces as well, as we noted in Figure 19. By contrast, when using DDES, similar levels of eddy-viscosity are not predicted by the model at the closure of the sheet cavity. We also note considerably more unsteady vortical flow structures with DDES, shed in the wake of the foil. Due to these reasons, the natural shedding of the sheet cavity did occur as was demonstrated in Sections 4.2 and 4.3.

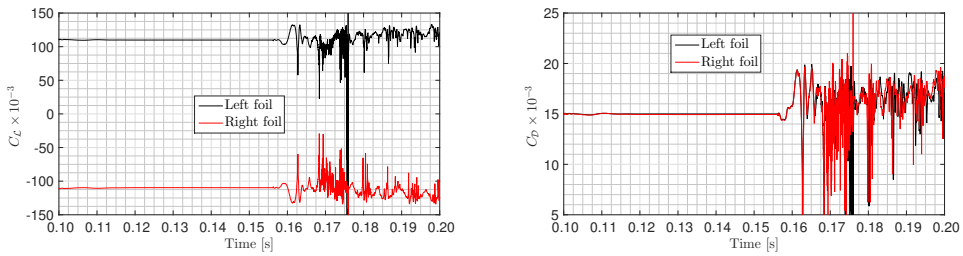

(**a**) Lift coefficient. (**b**) Drag coefficient.

Figure 19. Illustration of an effect of DDES. Simulations were carried out using SST $k - \omega$ until $t \approx 0.155$ s, after which the DDES approach was activated. Medium grid, $U_\infty = 8$ m/s, $\sigma = 1.27$.

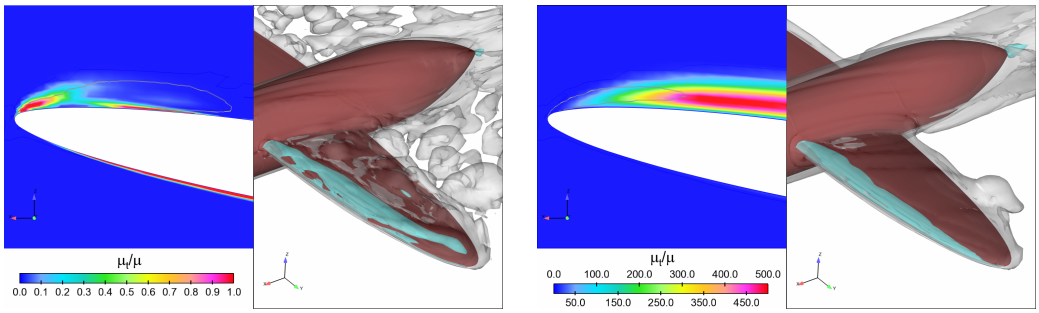

(**a**) DDES. (**b**) SST.

Figure 20. Snapshots of simulations with DDES and SST. Medium grid, $\sigma = 1.27$. Left frame depicts a cut plane of the left foil at mid-span with the contour of void fraction $\alpha = 0.1$ denoted by the grey curves, and the plane is colored by the eddy-viscosity ratio. The right frame shows the cavity extent near the left foil by an iso-surface of the void fraction $\alpha = 0.1$, colored by light blue, and vortical flow structures by an iso-surface of $|\Omega_i| = 300\ 1/s$ as the transparent grey color.

We note here the natural shedding behavior of the case with lower cavitation number was reasonably captured also with the used URANS approach, as discussed in Section 4.2 and seen in Figures 10 and 11. This observation might be because the foil was, in an average sense, at a super-cavitating state where the attached sheet cavitation momentarily covered the entire suction side of the foil. It appears that in this case the shedding mechanism is strong enough to overcome the, perhaps excess, diffusion originating from the eddy-viscosity modelling even on the medium grid.

5. Conclusions

We studied the ITTC Standard Cavitator numerically in a cavitation tunnel at different cavitation numbers. To our knowledge, our numerical analyses are the first reported ones for the ITTC standard cavitator. Emphasis was put upon the assessment of sheet-cavitation dynamics. A compressible two-phase flow model was used for the flow solution, and two turbulence closures are employed: a two-equation RANS model, SST $k - \omega$, and a hybrid RANS/LES model, called the delayed-detached eddy simulation (DDES). A homogeneous mixture model was used for the two phases.

We compared the simulations with observations made in the cavitation tunnel experiments. Good agreement was achieved with the mean cavitation extent, in terms of the sheet cavitation on the foils, and the hub vortex cavitation which formed behind the cavitator body. The numerically predicted sheet-cavitation shedding frequencies can also be observed with some hydrophones in the acoustic measurements, which were carried out in the cavitation tunnel. Streak cavitation at the hemispherical head of the cavitator body was predicted as an attached sheet cavitation in the simulations. The numerical grid resolution did not permit the capturing of the very fine tip vortex cavitation that was observed in the experiments. Also, the prediction of flows with bubble cavitation is difficult with a homogeneous two-phase mixture model.

Detailed analysis of the cavitation shedding mechanism confirmed that the dynamics of the sheet cavitation are dictated by the re-entrant jet. Once the jet impinges the sheet cavitation, a detachment takes place together with complex interaction between the re-entrant jet, vortical flow structures and mass transfer near the phase boundary. We observed that the break-off cycle was relatively periodic in both investigated cases with an approximately constant shedding frequency. The Strouhal numbers lay within the usual ranges reported in the literature for sheet-cavitation shedding. Furthermore, we noted that a strong vortical flow formed around the detached cavity. In the case of the lower cavitation number, we demonstrated that the vortical flow structures convected to the slipstream of the foils, where they developed striking cavitating toroidal vortices. An intricate interplay with the shed vapor clouds and the liquid-phase flow introduced vast vortical flow structures when the sheet cavity detachment took place. We showed that once the toroidal vortex ring was formed, the vorticity was in

most parts strong enough for the flow inside the vortex rings to cavitate. Furthermore, a collapse event of a cavity cloud in the slipstream of the foils gave rise to a considerable pressure peak and subsequent wave-like fronts.

DDES and simulations with the URANS model revealed a difference of approximately 5 Hz in the sheet-cavitation shedding for the case with the lower cavitation number. The shedding behavior was reasonably captured also with a two-equation turbulence model. This observation might be because the foil was, in an average sense, at a super-cavitating state where the attached sheet cavitation momentarily covered the entire suction side of the foil. It appears that in this case the shedding mechanism is strong enough to overcome the, perhaps excess, diffusion originating from the eddy-viscosity modelling even on the rather coarse grids. For the case with the higher cavitation number, the two-equation turbulence model predicted a steady attached sheet cavitation, whereas the hybrid RANS/LES model predicted a highly transient sheet-cavitation shedding being on a par with the experiments. We attributed this difference to the eddy-viscosity modelling. In this case, detailed vortical structures around the foil and the shedding mechanisms of the sheet cavitation were inhibited due to the unsteady RANS modelling approach.

Recently we have investigated the Reynolds number sensitiveness of different cavitation types observed on a ship's propeller [31]. For the case of static hydrofoils exhibiting similar phenomena as shown here, this remains to be assessed. Moreover, the ability of an asymptotic mass-transfer model coupled to the compressible flow solver to predict the shock wave dynamics, which can have an effect on the upstream cavitation dynamics [1], remains an open issue. One alternative is to include the Rayleigh–Plesset equation, which takes the bubble dynamics better into account, to the flow model for a more complete physical description of the two-phase flow. Other options to achieve better results comprise more holistic modelling approaches that can better account for the phase change physics, such as inhomogeneous or multi-scale flow models. An extended model of the former type is under development by the authors, and we have obtained promising initial results of propeller cavitation using such an approach.

Author Contributions: Conceptualization, V.M.V., T.S. (Timo Siikonen), A.S.-C. and T.S. (Tuomas Sipilä); methodology, V.M.V. and T.S. (Tuomas Sipilä); software, V.M.V. and T.S. (Timo Siikonen); validation, V.M.V.; formal analysis, V.M.V.; investigation, V.M.V.; resources, V.M.V. and T.S. (Tuomas Sipilä); data curation, V.M.V. and T.S. (Timo Siikonen); writing—original draft preparation, V.M.V.; writing—review and editing, T.S. (Timo Siikonen), A.S.-C. and T.S. (Tuomas Sipilä); visualization, V.M.V.; supervision, T.S. (Timo Siikonen), A.S.-C. and T.S. (Tuomas Sipilä); project administration, T.S. (Tuomas Sipilä); funding acquisition, T.S. (Tuomas Sipilä). All authors have read and agreed to the published version of the manuscript.

Funding: V.M.V. would like to express his gratitude for the support granted by the Finnish Funding Agency for Innovation (TEKES) and the German Federal Ministry for Economic Affairs and Energy within the project "PropNoise". Without the funding the research project could not have been realized. The APC was funded by VTT.

Acknowledgments: The authors would like to express their gratitude to Rhena Klose and Lars Lübke from SVA Potsdam GmbH for providing the experimental results and photographs.

Conflicts of Interest: The authors declare no conflict of interest. The funders had no role in the design of the study; in the collection, analyses, or interpretation of data; in the writing of the manuscript, or in the decision to publish the results.

Abbreviations

The following abbreviations are used in this manuscript:

CFD	Computational fluid dynamics
DES	Detached-eddy simulation
DDES	Delayed DES
ITTC	International Towing Tank Committee
LE	Leading edge
LES	Large eddy simulation
MUSCL	Monotonic upstream-centered scheme for conservation laws

RANS	Reynolds-averaged Navier–Stokes
SST	Shear stress transport
TE	Trailing edge
URANS	Unsteady RANS

References

1. Ganesh, H.; Mäkiharju, S.; Ceccio, S. Bubbly shock propagation as a mechanism for sheet-to-cloud transition of partial cavities. *J. Fluid Mech.* **2016**, *802*, 37. [CrossRef]
2. Schnerr, G.H.; Sezal, I.; Schmidt, S. Numerical investigation of three-dimensional cloud cavitation with special emphasis on collapse induced shock dynamics. *Phys. Fluids* **2008**, *20*, 040703. [CrossRef]
3. Sipilä, T. RANS Analyses of Cavitating Propeller Flows. Ph.D. Thesis, School of Engineering, Aalto University, Espoo, Finland, 2012.
4. Dular, M.; Bachert, R. The issue of Strouhal number definition in cavitating flow. *J. Mech. Eng.* **2009**, *55*, 666–674.
5. Lei, W.; Lu, C.J.; Jie, L.; Xin, C. Numerical simulations of 2D periodic unsteady cavitating flows. *J. Hydrodyn. Ser. B* **2006**, *18*, 341–344.
6. Saito, Y.; Nakamori, I.; Ikohagi, T. Numerical analysis of unsteady vaporous cavitating flow around a hydrofoil. In Proceedings of the 5th International Symposium on Cavitation (CAV2003), Osaka, Japan, 1–4 November 2003.
7. Leroux, J.B.; Coutier-Delgosha, O.; Astolfi, J. A joint experimental and numerical study of mechanisms associated to instability of partial cavitation on two-dimensional hydrofoil. *Phys. Fluids* **2005**, *17*, 052101. [CrossRef]
8. Matusiak, J. Pressure and Noise Induced by a Cavitating Marine Screw Propeller. Ph.D. Thesis, Helsinki University of Technology, Espoo, Finland, 1992.
9. Gnanaskandan, A.; Mahesh, K. Large eddy simulation of the transition from sheet to cloud cavitation over a wedge. *Int. J. Multiph. Flow* **2016**, *83*, 86–102. [CrossRef]
10. Eskilsson, C.; Bensow, R.E. Estimation of Cavitation Erosion Intensity Using CFD: Numerical Comparison of Three Different Methods. In Proceedings of the Fourth International Symposium on Marine Propulsors (smp'15), Austin, TX, USA, 31 May–4 June 2015.
11. Bensow, R.; Bark, G. Implicit LES predictions of the cavitating flow on a propeller. *J. Fluids Eng.* **2010**, *132*. [CrossRef]
12. Viitanen, V.M.; Hynninen, A.; Sipilä, T.; Siikonen, T. DDES of Wetted and Cavitating Marine Propeller for CHA Underwater Noise Assessment. *J. Mar. Sci. Eng.* **2018**, *6*, 56. [CrossRef]
13. Sakamoto, N.; Kamiirisa, H. Prediction of near field propeller cavitation noise by viscous CFD with semi-empirical approach and its validation in model and full scale. *Ocean Eng.* **2018**, *168*, 41–59. [CrossRef]
14. Ge, M.; Svennberg, U.; Bensow, R. Investigation on RANS prediction of propeller induced pressure pulses and sheet-tip cavitation interactions in behind hull condition. *Ocean Eng.* **2020**, *209*, 107503. [CrossRef]
15. Morgut, M.; Nobile, E.; Biluš, I. Comparison of mass transfer models for the numerical prediction of sheet cavitation around a hydrofoil. *Int. J. Multiph. Flow* **2011**, *37*, 620–626. [CrossRef]
16. Li, Z.; Pourquie, M.; Van Terwisga, T. A numerical study of steady and unsteady cavitation on a 2d hydrofoil. *J. Hydrodyn.* **2010**, *22*, 728–735. [CrossRef]
17. Ducoin, A.; Huang, B.; Young, Y.L. Numerical modeling of unsteady cavitating flows around a stationary hydrofoil. *Int. J. Rotating Mach.* **2012**, *2012*. [CrossRef]
18. Wang, C.; Wang, G.; Huang, B. Characteristics and dynamics of compressible cavitating flows with special emphasis on compressibility effects. *Int. J. Multiph. Flow* **2020**, *130*, 103357. [CrossRef]
19. Park, S.; Seok, W.; Park, S.; Rhee, S.; Choe, Y.; Kim, C.; Kim, J.H.; Ahn, B.K. Compressibility Effects on Cavity Dynamics behind a Two-Dimensional Wedge. *J. Mar. Sci. Eng.* **2020**, *8*, 39. [CrossRef]
20. Zhang, W.; Bai, X.; Ma, Z.; Chen, G.; Wang, Y. Compressible effect on the cavitating flow: A numeric study. *J. Hydrodyn. Ser. B* **2017**, *29*, 1089–1092. [CrossRef]
21. Budich, B.; Schmidt, S.J.; Adams, N.A. Numerical Investigation of a Cavitating Model Propeller Including Compressible Shock Wave Dynamics. In Proceedings of the Fourth International Symposium on Marine Propulsors (smp'15), Austin, TX, USA, 31 May–4 June 2015.

22. ITTC. Report of Cavitation Committee. In Proceedings of the 14th International Towing Tank Conference (ITTC), Ottawa, ON, Canada, 10–12 September 1975.
23. Miettinen, A.; Siikonen, T. Application of pressure- and density-based methods for different flow speeds. *Int. J. Numer. Methods Fluids* **2015**, *79*, 243–267. [CrossRef]
24. Viitanen, V.M.; Siikonen, T. Numerical simulation of cavitating marine propeller flows. In Proceedings of the 9th National Conference on Computational Mechanics (MekIT'17), Trondheim, Norway, 11–12 May 2017; International Center for Numerical Methods in Engineering (CIMNE): Barcelona, Spain, 2017; pp. 385–409, ISBN 978-84-947311-1-2.
25. Miettinen, A. *Simple Polynomial Fittings for Steam*; CFD/THERMO-55-2007; Report 55; Laboratory of Applied Thermodynamics, Aalto University: Espoo, Finland, 2007.
26. Spalart, P.R.; Deck, S.; Shur, M.; Squires, K.; Strelets, M.K.; Travin, A. A new version of detached-eddy simulation, resistant to ambiguous grid densities. *Theor. Comput. Fluid Dyn.* **2006**, *20*, 181–195. [CrossRef]
27. Menter, F.R. Two-equation eddy-viscosity turbulence models for engineering applications. *AIAA J.* **1994**, *32*, 1598–1605. [CrossRef]
28. Menter, F. Influence of freestream values on k-ω turbulence model predictions. *AIAA J.* **1992**, *30*, 1657–1659. [CrossRef]
29. Shur, M.; Spalart, P.; Strelets, M.; Travin, A. Detached-Eddy Simulation of an Airfoil at High Angle of Attack. In *Engineering Turbulence Modelling and Experiments 4*; Elsevier Science Ltd.: Oxford, UK, 1999; pp. 669–678.
30. Choi, Y.H.; Merkle, C.L. The application of preconditioning in viscous flows. *J. Comput. Phys.* **1993**, *105*, 207–230. [CrossRef]
31. Viitanen, V.; Siikonen, T.; Sánchez-Caja, A. Cavitation on Model-and Full-Scale Marine Propellers: Steady and Transient Viscous Flow Simulations At Different Reynolds Numbers. *J. Mar. Sci. Eng.* **2020**, *8*, 141. [CrossRef]
32. Klose, R.; Heinke, H. *Cavitation Tests and Noise Measurements with the Static Hydrofoil (ITTC Standard Cavitator)*; SVA Potsdam, Germany, Model Basin Report No. 4542; SVA (Potsdam Model Basin): Potsdam, Germany, 2017.